Adaptive notch- filtration to effectively recover photoplethysmographic signals during physical activity

Graphical Abstract

Adaptive notch-filtration to effectively recover photoplethysmographic signals during physical activity

Xiaoyu Zheng, Vincent Dwyer, Mahsa Derakhshani, Laura Barrett, Sijung Hu

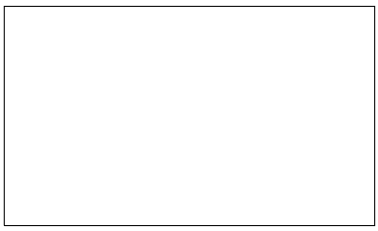

Highlights

Adaptive notch-filtration to effectively recover photoplethysmographic signals during physical activity

Xiaoyu Zheng, Vincent Dwyer, Mahsa Derakhshani, Laura Barrett, Sijung Hu

- Low-complexity PPG signal recovery algorithm for real-time health monitoring and assessment in wearable system.
- Development of ANF for the effective removal of in-band and out-of-band motion artefact at various physical activity intensities.
- Improved HR and RR values as obtained from the protocol implementation at four stages of cycling and treadmill exercises with 24 subjects .
- A smaller absolute error in HR and RR values, using the proposed signal processing technique, than by other published methods.

Adaptive notch-filtration to effectively recover photoplethysmographic signals during physical activity

Xiaoyu Zheng[a], Vincent Dwyer[a], Mahsa Derakhshani[a], Laura Barrett[b], Sijung Hu[a,*]

[a] *Wolfson School of Mechanical, Electrical, and Manufacturing Engineering, Loughborough University, Loughborough, LE11 3TU, UK*
[b] *School of Sport, Exercise and Health Sciences, Loughborough University, Loughborough, LE11 3TU, UK*

Abstract

Physical activity can severely influence the quality of photoplethysmographic (PPG) signals due to motion artefacts (MA). This study aims to extract heart rate (HR) and respiration rate (RR) values from raw PPG signals captured from a multi-wavelength illumination optoelectronic patch sensor (mOEPS) during physical activity of different intensities, and to do this in an effective manner. The proposed method, combined with a 3-axis accelerometer as a motion reference, was developed for the extraction of the desired PPG signals. The overall algorithm comprises three parts: 1) the adaptive moving average filter, 2) the adaptive notch filter, and 3) the physiological parameter extraction. 24 healthy subjects completed four stages of exercise of increasing intensity, first on a cycle ergometer and later on a treadmill. The recovered PPG signals for the calculation of HR and RR were comparable to the measurements from commercial devices, with an average absolute error for HR of <1.0 beats/min for the IEEE-SPC dataset, and 1.3 beats/min for HR, and 2.8 breaths/min for RR, from the in-house dataset obtained at Loughborough University. The method used is found to have good robustness and low complexity, making it suitable for application in real-time physiological monitoring.

Keywords: motion artefacts (MA), multi-wavelength illumination optoelectronic patch sensor (mOEPS), adaptive notch-filtration (ANF),

*Corresponding author
Email address: S.Hu@lboro.ac.uk (Sijung Hu)

1. Introduction

Photoplethysmography (PPG) as a low-cost, non-invasive, and optical technique is usually used to measure vital physiological signs, such as heart rate, heart rate variability, oxygen saturation, and respiration rate [1]. As a consequence PPG-based health monitoring has been widely adopted for wearable devices [2, 3]. The periodic variations in the PPG signal, related to the cardiac rhythm and breathing changes, make it possible to determine heart rate (HR) and respiration rate (RR) [4, 5]. Despite the wealth of physiological information that the PPG signal can provide, it is easily disturbed by artefact noise generated from a variety of noise sources, such as: modification of the optical properties of the internal tissues; poor blood perfusion; motion artefacts (MA); the distance between the optical sensor and skin surface, and electromagnetic and electronic noise [6, 7].

Heart rate and RR calculations from noise artefact-induced PPG signals have been acquired accurately, using a number of different methods including independent component analysis (ICA) [8], frequency-domain ICA [9], empirical mode decomposition (EMD) [10], improved complete ensemble empirical mode decomposition with adaptive noise (ICEEMDAN) [11], a wavelet-transform method [12] and Kalman filtering [13]. However, these methods are generally only suitable for relatively low-intensity movement [14]. The relationship between acceleration and the PPG signals has also been exploited to extract PPG signals in the case of low intensity MA [15]. Subsequently, acceleration data has become the a versatile aid for the removal of MAs. An adaptive noise cancellation method using recursive least squares (RLS) [16] and an adaptive-size least mean squares (AS-LMS) adaptive filter [17] have been applied to weaken the noise artefacts with the aid of acceleration measurements which are associated with the intensity of motion. These adaptive filtering (AF) methods have proved to have better properties at low-intensity than at high-intensity exercise [18]. The performance of AF is highly associated with the quality of reference signal, i.e., acceleration signal) as is linearly related to the MAs. Such AF is uneasily applied for a real-time MAs cancellation [19].

To overcome these shortcomings, Zheng et al. [20] proposed an effective method (TROIKA) to remove MA from wrist-worn PPG, which has a better

noise removal ability and robustness. Yet, this method based on the sparse signal decomposition is not sufficiently accurate for extracting HR. Meanwhile, TROIKA was improved by the joint sparse spectrum reconstruction (JOSS) [21], by exploiting the fact that the spectra of PPG signals and 3-axis acceleration signals have common features, to generate a spectral estimation of these signal as a JOSS model. Although the JOSS method can effectively remove in-band MAs in low and high-intensity motions, it cannot be used during real-time monitoring due to its high computational complexity. A time-varying spectral filtering algorithm has been recently developed in [22], which compares the frequency of the PPG spectrum with the acceleration spectra. These frequency peaks generated by MAs can be distinguished from the PPG spectrum. Due to the demand of larger data processing capacity for sample-by-sample windowing process, it may be uneasy to deploy the algorithm into a wearable electronic system for a real-time recovery of PPG signals. Lately, Islam et al.[23] introduced a modified spectral subtraction scheme with a composite motion artifact reference (SPECMAR) method along with a synthetic motion artefacts reference. Again, a fusion method was reported in [1], using band-stop filters to remove the in-band MAs. The method then applies the band-stop filter with a rejection frequency related to the acceleration spectrum under static conditions, which can be easily achieved on a primary processor platform.

Referring to these methods, the purpose of this study is to explore how to effectively recover PPG signal against MA corruption in order to extract physiological parameters in real-time. To achieve this, an adaptive notch-filtration algorithm (ANF) was established as a practicable signal processing platform and developed for reduction of MAs in different physical activity intensities in order to recover cleansed PPG signals. The ANF is intended for real-time use, the filtration algorithm has low complexity but still allows accurate physiological readings. The study includes the following aspects:

1) The proposed ANF to be effectively applied for the in-band and out-of-band MA at different exercise intensities , to obtain MA-free PPG signals.
2) The better HR and RR readings to be worked out from the recovered PPG signals by the means of ANF.
3) The smaller absolute error values to be delivered by the ANF along with a 24 subject engaged protocol in different physical exercises levels.
4) The deploy of ANF into a wearable electronic system to be durable to achieve an indeed real-time health monitoring.

2. Methods and Materials

The block diagram of the proposed ANF executive is depicted in Fig.1. The proposed method consists of three essential parts: 1) the adaptive moving average filter (AMAF), 2) the adaptive notch filter, and 3) physiological parameters extraction. Firstly, a smoothing process on the raw PPG signals is performed, adopting an AMAF for the purpose of removing the out-of-band noise caused by the poor attached sensor, external electromagnetic impact or low blood perfusion. Secondly, the adaptive notch filter is employed to remove the in-band MA from the filtered PPG signals with the aid of the 3-axis acceleration signals by finding a set of peaks from the frequency spectrum of the cleaned signals. Finally, the algorithm to extract physiological parameters (here HR and RR) was designed to ensure that accuracy of those parameters from the recovered PPG signals show an improvement on previous work. In the following sections, the overall algorithm (ANF) is presented in detail.

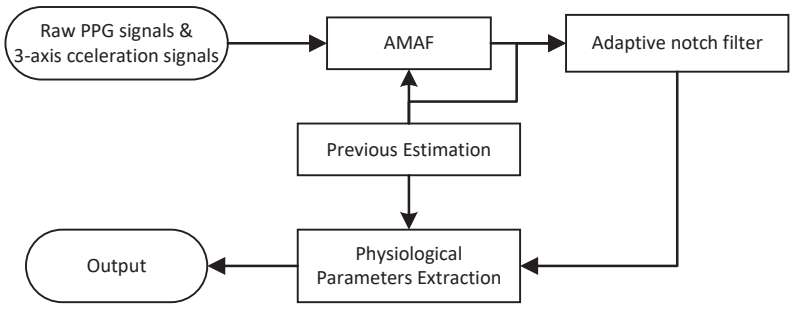

Fig. 1. Block diagram of the ANF executive

2.1. Adaptive Moving Average Filter (AMAF)

Prior to the procedure of the ANF, 3-axis acceleration signals are selected through a 4th Butterworth band-pass filter with cut-off frequencies of 0.2 and 6 Hz. The signals are then subjected to Fast Fourier Transform (FFT). The raw PPG signals obtained from green illumination of the OEPS are usually first filtered using an adaptive moving average filter (AMAF). To obtain a better signals, fitting parameter is often adapted automatically during physiological measurement period for various sliding windows. The input signal sequences is $S_{\text{in}} = [s_1, s_2, s_3, \ldots, s_n]$ and the fitting parameter is p. The input raw data sequence is smoothed by a simple background subtraction using

the p-point moving average filter. The output S_{out} at the current point i is represented by the mean from the $(i - p/2)^{th}$ to $(i + p/2 - 1)^{th}$ points as below:

$$S_{\text{out}}(i) = \frac{1}{p} \sum_{k=i-p/2}^{i+p/2-1} (S_{\text{in}}(i) - S_{\text{in}}(k)). \tag{1}$$

For an arbitrary frequency component, $S_{in}(i) = \exp(2\pi jfn/F_s)$, in the measured raw data, the output obtained from the AMAF S_{out} is modified to

$$\begin{aligned} S_{\text{out}}(i) &= \exp(2\pi jfn/F_s)\left(1 - \frac{\exp(2\pi jfp/2F_s) + ... + 1 + ... + \exp(-2\pi jf(p/2-1)/F_s)}{p}\right) \\ &\approx \exp(2\pi jfn/F_s)\left(1 - \text{sinc}\Big(pf/F_s\Big)\right) \\ &= H_{AMAF}(f;p)\exp(2\pi jfn/F_s). \end{aligned} \tag{2}$$

$H_{AMAF}(f;p)$ represents an adaptive high-pass filter, with an adaptation parameter p, and a cut-off frequency of $f \approx F_s/p \approx 256/p$ Hz with the current sample rate of $F_s = 256$ Hz. Choosing $p = 256$ samples would ensure all Heart Rates > 60 beats/min not be cut off. Similarly, p should be reduced to ≈ 64, or a cutoff of 15 breaths/min, when calculating RR.

With the time variation of HR or RR, the bandwidth of the AMAF filter window must adjust (under adaptation) to reflect the change. We set up the adaptation rule in a manner that keeps the value $H_{AMAF}(f_{HR/RR})$ roughly fixed, i.e.,$pf_{HR/RR}/F_s \approx 1$. This is implemented, for the m^{th} interval, by using the frequency of previous HR or RR as, thus

$$\frac{p(m) \times f_{HR/RR}(m-1)}{F_s} = 1. \tag{3}$$

where all frequencies are in Hz. In this way $p = 256$ is used in the case that $f_{HR} = 1$Hz. After the above procedure, a digital FIR band-pass filter acts on the S_{out} to remove the out-band noise impact with the same cut-off frequencies of 0.2 to 6Hz as earlier.

2.2. Adaptive Notch Filter for In-band Motion Artefacts Removal

To further remove MAs, the pre-processed PPG signal, along with 3-axis acceleration references, are loaded into the signal processing system, here

denoted as ANF and shown in Fig.2. Suitable notch filters are selected in each sliding time window rather than using a fixed notch filter, as in [1].

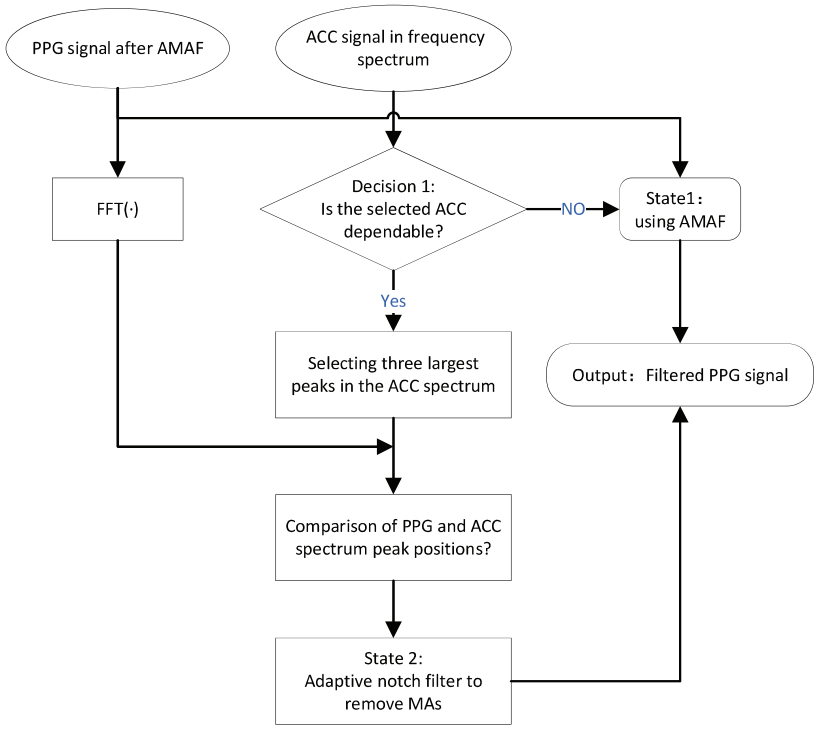

Fig. 2. The flowchart of the adaptive notch filter

Prior to processing with the ANF, the acceleration signal (ACC) is chosen as a reference noise signal in each sliding time window. Precisely, to minimize the complexity of ANF, the analysis of only one axis (i.e., x-axis) of the acceleration signal was considered [1]. Next, it needs to be verified whether the peaks in the ACC spectrum are related to MAs; such peaks are expected to present as fairly large during strenuous exercise. When the 3-axis acceleration spectrum is too broad, the useful MA component cannot easily be extracted by exploring the acceleration signal. Thus, Decision 1 is adopted to check the largest spectral peak in the selected acceleration data as shown in Fig.2. When the largest spectral peak is less than some threshold (th_1), it indicates that the current motion state is not significant to feed through to the PPG signal and the MA interference is relatively trivial. Again, th_1 is the critical threshold between exercise and rest. It is obvious that the N_{FFT}-

point FFT with zero paddings was adopted to arrive at the ACC spectrum, thus th_1 (i.e. the value of 50) would be estimated according to the sampling rate and N_{FFT}. In this case, the AMAF filtered PPG signal is used as the algorithm output (State 1). Thus, the ACC signal is unnecessary in this sliding time window, and State 2 is triggered as detailed below.

The 2nd infinite impulse response (IIR) filter is also introduced to implement the notch filter in State 2, which is always stable and has a linear delay [24]. The notch filter general transfer function [25] is shown as:

$$H(z) = \frac{r^2 - (1 + r^2)\cos(\omega)z^{-1} + z^{-2}}{1 - (1 + r^2)\cos(\omega) + r^2 z^{-2}}, \tag{4}$$

where

$$\omega = \frac{2f_c}{f_s}, r = \frac{f_c}{\mu}. \tag{5}$$

In (4) and (5), r controls the bandwidth of the notch filter and μ is the bandwidth coefficient, f_c is the central frequency of the notch filter and f_s is the signal sampling rate. The magnitude response of the notch filter is illustrated in Fig.3. As can be seen from the graphs, the parameter ω controls the bandwidth of the notch filter, and the notch filter removes the signal around notch frequencies while keeping the other frequency components close to their original amplitudes.

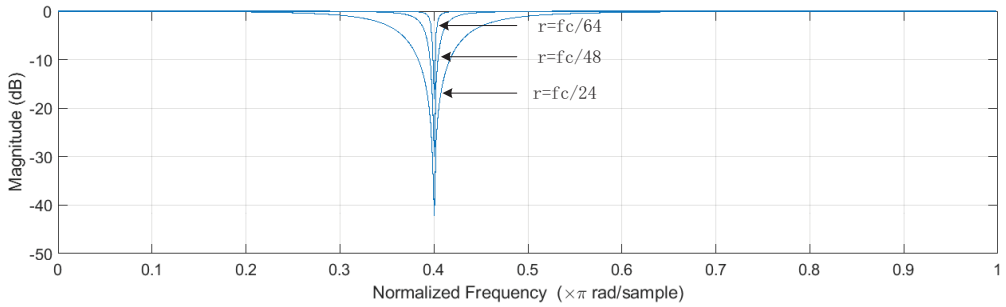

Fig. 3. Magnitude responses of the notch filter

Suppose that f_{a_1}, f_{a_2} and f_{a_3} are the location indexes of the top three ACC spectrum peaks, which are also the central rejection frequencies of the notch filters. In the proposed algorithm, for a central rejection frequency f_a, f_a/μ is assumed to be the bandwidth of the notch filter and μ is set to 48. The general equation for a notch filter is expressed by

$$H_{notch}(f; f_a) = \begin{cases} \delta, & \Big(1 - 1/\mu\Big) f_a \leq f \leq \Big(1 + 1/\mu\Big) f_a. \\ 1, & \text{otherwise.} \end{cases} \tag{6}$$

where $\delta \ll 1$ and f_a stands for f_{a_1}, f_{a_2} or f_{a_3}.

Next, the notch filter, which has adaptive rejection frequencies chosen based on the different scenarios, is applied to the PPG signal recovered in each time window. In the following, we discuss different ANF scenarios considering cases where the spectral peaks indicating the desired physiological parameters (i.e., HR and RR) are located on the first, second or third PPG spectrum peaks, depending on which PPG peak is closest to the previous calculated physiological parameter value. Here the spectral peak selected to represent the related physiological parameter is labelled f_{sel}.

- **Scenario 1:** f_{sel} isn't taken account for the overlap with any of the three largest ACC spectrum peaks, and so is not affected by the notch filter. Precisely, the peak of the PPG spectrum corresponding to the HR or RR frequency does not coincide with the three leading ACC spectral peaks. In this case, the ANF is comprised of the three notch filters, and is demonstrated in Fig.4. There, Fig.4(a2) and (b2) shows the measured PPG signal corrupted with MAs. As is apparent, features of the PPG signal in the time-domain (and in the frequency-domain) are poor. It is necessary to remove the frequencies from the MAs that are related to the ACC reference, these are marked by red circles in Fig.4(a1) and Fig.4(a1).

- **Scenario 2:** f_{sel} is taken account for the overlap with one of the three largest of the ACC spectral peaks. Fig.5(a2) shows an example case in which the physiological parameter frequency (indicated by the black circle) overlaps with the largest of the ACC spectral peak. Continuing with the ANF from scenario 1 would filter out the true HR (or RR) frequency, and not recover the desired PPG signals in the time-domain as is illustrated in Fig.5(a3) and (b3). Clearly this spectral peak should be retained, but the other MA related spectrum peak should be removed. The recovered PPG signal in this case is illustrated in Fig.5(a4) and (b4). These two scenarios can be pressed as the function of ANF as shown below:

$$H_{ANF}(f) = \begin{cases} \prod_{k\in\{1,2,3\}} H_{notch}(f; f_{ak}), & F_{HR/RR} \approx\!\!\!\approx f_{aj}. \\ \prod_{k\neq j, \in\{1,2,3\}} H_{notch}(f; f_{ak}), & F_{HR/RR} \approx f_{aj}. \end{cases} \tag{7}$$

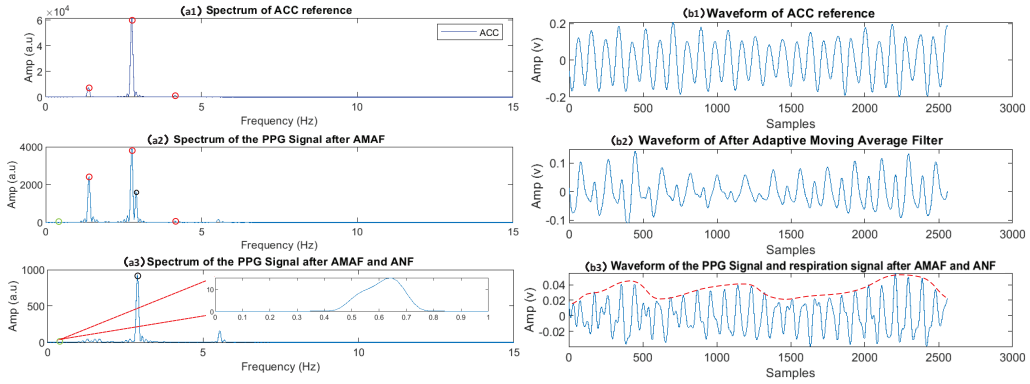

Fig. 4. Detailed processing for the PPG signal when frequencies of the MAs are in-band of the PPG signal in Scenario 1. (a1) ACC spectrum peaks as the reference for MAs. (b2) ACC signals in time-domain. (a2) corrupted PPG signals with the MAs, and the red circle marks coincide with the three most significant spectrum peaks of ACC, and the black and green circles correspond to the frequency of HR and RR. (b2) filtered PPG signals after AMAF in time-domain. (a3) desired PPG signals and respiration signals spectrums. (b3) recovered PPG signals and respiration signals after AMAF and ANF.

2.3. Physiological Parameters Extraction

2.3.1. Heart Rate Extraction

Usually, the identified MAs are removed and the cleaned PPG signals are recovered effectively in the previous steps. However, in some cases, the sensor may barely capture the PPG signal; for example, if the sensor contact is loose. Thus, a spectral peak calibration and selection are crucial for accurate HR/RR extraction. Prior to these two steps, the HR is calculated as $HR_{BPM} = f_{sel} \times 60$ beats/min, and similarly RR.

(1) **Calibration:** Calibration mainly ensures that the filtered PPG signals are still adversely affected by motion. Typically the change in the HR, between successive sliding time window observations, is expected to be limited. Accordingly the following check is performed.

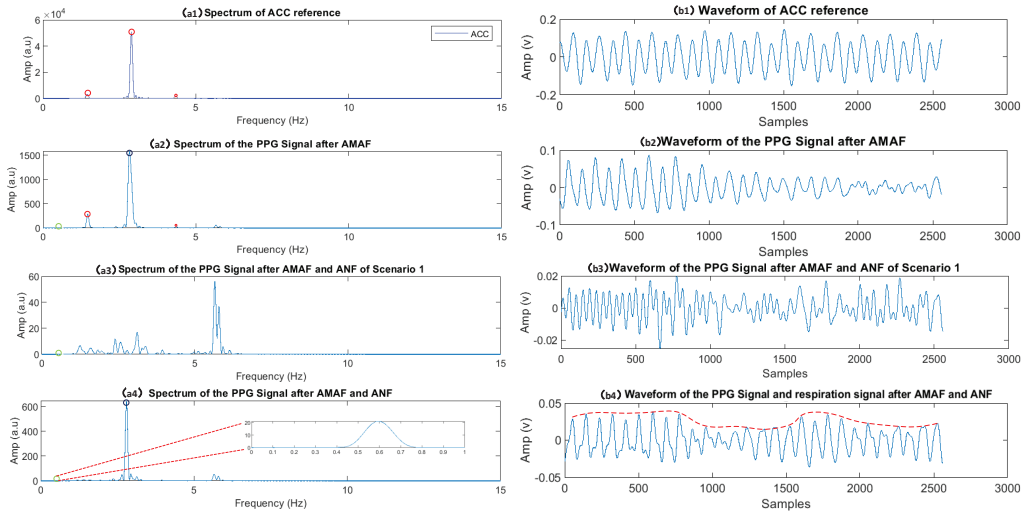

Fig. 5. Detailed processing for the PPG signal when frequencies of the MAs are in-band of the PPG signal in Scenario 2. (a1) ACC spectrum peaks as the reference for MAs. (b2) ACC signals in time-domain. (a2) corrupted PPG signals with the MAs, and red and black circle marks overlap with the three largest ACC spectrum peaks, but the black and green circles correspond to the frequency of HR and RR. (a3) applying the ANF bandwidth of scenario 1. (b3) its corresponding time-domain waveform. (a4) desired PPG signals and respiration signals spectrums. (b4) its corresponding time-domain waveform.

$$|HR_{BPM}[i] - HR_{BPM}[i-1]| < \phi, \tag{8}$$

where ϕ is a tolerance parameter, ensuring that the difference between the current time window heart rate and previous value is within a reasonable tolerance ($\phi = 5beats/min$). When the rule is satisfied, the current HR_{BPM} is selected as the final calculated HR. Otherwise, the algorithm moves on to the last part, Selection.

(2) **Selection:** The selection deals with the situations that the verification rule (Eq. 8) is not satisfied. When no satisfactory f_{sel} can be found, the offending sliding time-window is skipped, and $HR_{BPM}[i]$ is estimated by the trend of the previous three HR values. Specifically, when the trend is upwards (i.e. $HR[i-3] \leq HR[i-2] \leq HR[i-1])$), $HR_{BPM}[i]$ is set to $HR_{BPM}[i-1]+2$. Again, when the trend is down, $HR_{BPM}[i]$ is set to $HR_{BPM}[i-1]-2$. Otherwise, the $HR_{BPM}[i]$ is kept the same as previous heart rate, $HR_{BPM}[i-1]$. Finally, the output HR is the average value of the five previous HRs.

2.3.2. Respiration Rate Extraction

After removing the MAs from the PPG signals, the acceleration-derived method is used to extract RR [26]. Precisely, a motion intensity (MI) index is defined using the amplitudes of the 3-axis acceleration signal (ACC) (Amp_{ACC}).

$$MI = \begin{cases} \text{low} & Amp_{ACC} \leq 100, \\ \text{medium} & 100 < Amp_{ACC} \leq 400, \\ \text{high} & Amp_{ACC} > 400. \end{cases} \tag{9}$$

Again, the parameters of the band-pass filter are selected adaptively. When the MI is low, the passband of the band-pass filter is set to 0.2-0.5Hz; when MI is medium, the passband is set to 0.3-0.7 Hz and when MI is high the passband is set to 0.4-0.9. Thereafter, the RR can be obtained from the peak in the frequency domain FFT.

2.4. Parameter Settings

For the LU-Db dataset the sampling rate (F_s) is at 256 Hz, the time window sliding along the signals is 10 seconds long with HR values are (using the ANF) are extracted in 1s intervals, and the number of FFT points (N_{FFT}) is set to 8192. In general we recommended that N_{FFT} is set so that each frequency bin ($F_s/N_{FFT} \times 60$) corresponds to about 1 beats/min. By contrast for the IEEE-SPC dataset, the sampling rate is $F_s = 128Hz$ so N_{FFT} is set to 4096. Here, the time window is 8 seconds long with an incremental step of 2 seconds.

2.5. Measurement Protocol

The ANF was conducted with two databases: a) Loughborough University database (LU-Db) and b) IEEE Signal Processing Cup (SPC) 2015. LU-Db was well suited for the validation on two exercise forms with four different motion intensities, e.g., 1) cycling, and 2) running . The SPC database was used as a benchmark for verification of state-of-the-art signal processing algorithms. Specifically, with LU-Db, 12 healthy subjects (aged 24±3 years, two females and ten males) undertook the protocol which was approved by the Loughborough University Ethical Advisory Committee. During the protocol implementation, a reference of HR was recorded using a Polar Bluetooth® Smart chest strap (Polar, Electro, Kempele, Finland)) [27]. RR was also

determined using a VyntusTM CPX Metabolic cart (JAEGER(TM) Vyntus(TM) CPX, Carefusion, Germany). The OEPS sensor with 3-axis acceleration as a MA reference was placed on the subject thumb. During data recording, the subjects performed the following exercises: 1) cycling at four different levels of resistance 2) walking, and 3) running on a treadmill at different speeds . In these designated exercises, the female subjects cycled at 60, 90, 120 and 150 watts and the male subjects cycled at 90, 120, 150 and 180 watts, and all subjects walked or ran on a treadmill at 3, 6, 9 and 12 km/h for 4 min at each intensity with 1 min rest before the exercise intensity was increased. Fig.6 displays several subjects with the actual testing environment and equipment.

The IEEE-SPC database comprises of PPG signals of 5-minute duration from 12 healthy subjects aged 18 to 35 [20]. The dataset for each subject comprises one channel of PPG signals obtained from the OEPS corresponding with green LEDs (illumination wavelength: 525 nm), the 3-axis acceleration signals from the wrist, and the ECG signal from the chest using wet ECG sensors. During data recording, the subjects walked or ran on a treadmill with the following speeds in order: the running exercise at a speed of 6 km/h for a period of 60 s; again, the faster running exercise at a speed of 12 km/h for a period of 60 sec; the running exercise at a speed of 6 km/h for a period of 60 sec; then the faster running exercise at a speed of 12 km/h for a period of 60 sec and take 30 sec break.

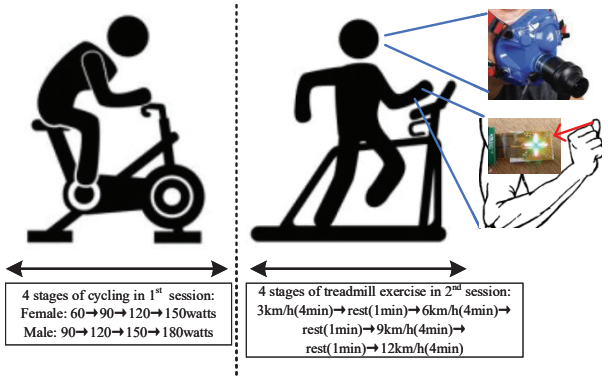

Fig. 6. Illustration of the exercise protocol during multi-stage cycle (1^{st} session) and treadmill (2^{nd} session) tests. The location of mOEPS sensor and respiration rate measurement sensor.

3. Results of Physiological Monitoring

3.1. Results Analysis

The results of continuous HR and RR monitoring of two different subjects in LU-Db dataset are presented by the ANF in Fig.7(a), Fig.7(b), Fig.8(a) and Fig.8(b). The ground-truth HR generated by the chest strap and the reference RR measured by the metabolic cart are also shown in Figs 7 and 8. It is observed that, for the ANF, the RR and HR performance is very robust, and highly accurate in tracking the reference RR and actual HR. In Fig.7, the blue shaded area represents the average RR at different exercise intensities, and it can be observed that the average RR increases as the motion intensity increases.

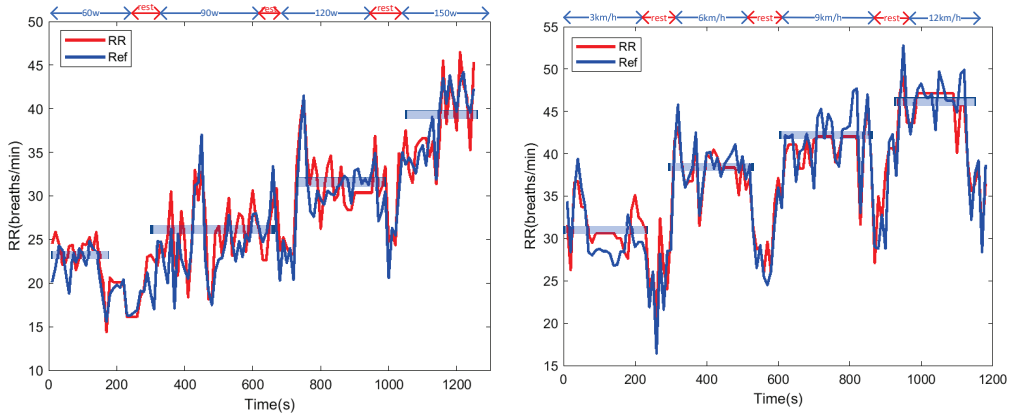

Fig. 7. RR calculation results on two subjects chosen LU-Db datasets. (a) The results of subject F03 in 1st session. (b) The results of subject M08 in 2nd session

Fig.9 and Fig.10 show that the detailed PPG signals in the time-domain correspond to the different motion intensity points as shown in Fig.8(a) and (b). (a1) is selected from the motion section with an intensity of 3km/h. Again, (a2), (a3) and (a4) are selected from running sessions at intensities of 6km/h, 9km/h and 12km/h respectively. (b1), (b2), (b3) and (b4) are chosen in the same way.

Table 1 expresses the average absolute error (ϵ_1) and the average error percentage (ϵ_2) for 12 subjects from the LU-Db datasets, 1st and 2nd sessions are listed, respectively. Satisfactory results are attained by using the ANF. In the 1st session, through an average of all 12 subjects' recordings, the average $\epsilon_1 = 1.07 \pm 0.17$ beats/min (mean $\pm$ std), and the average $\epsilon_2 = 1.04\%$.

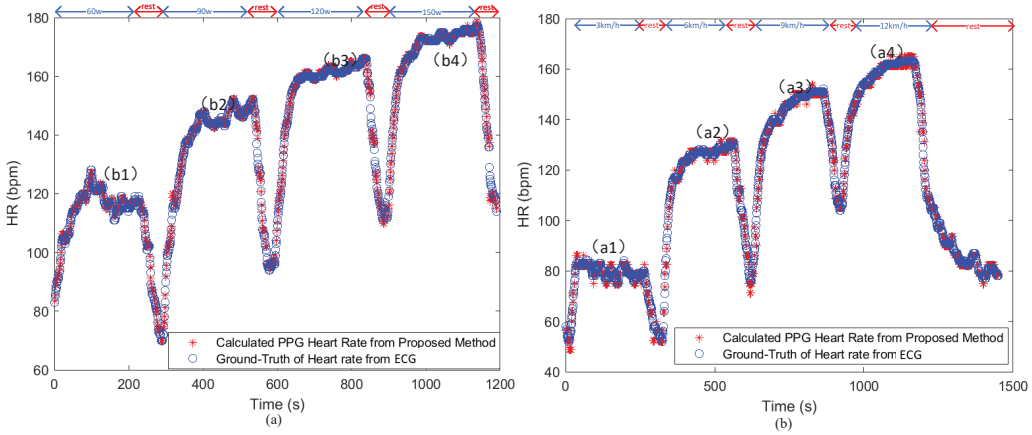

Fig. 8. HR calculation results on two subjects chosen LU-Db datasets. (a) The results of subject F03 in 1st session. (b) The results of subject M08 in 2nd session

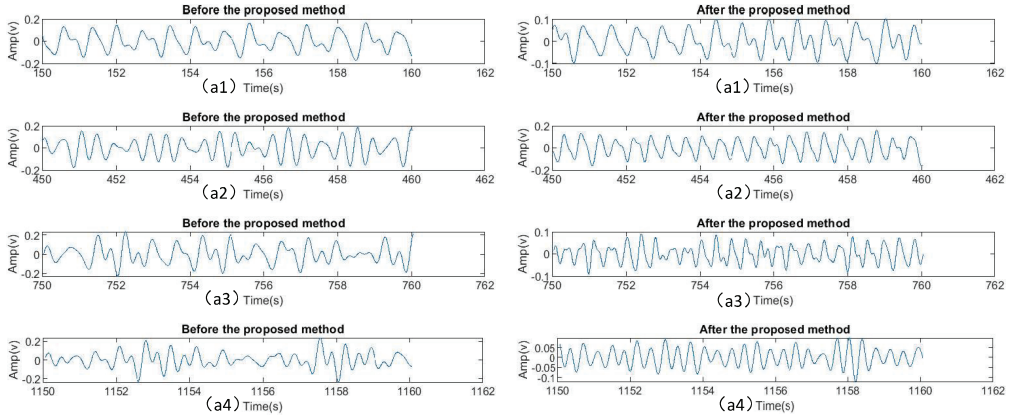

Fig. 9. Detailed PPG signals in the time domain correspond to different points in Fig.8(a).

Furthermore, in the 2nd session, the average ϵ_1 is 1.50±0.28 beats/min (mean ± std), and the average ϵ_2 is 1.26%. The Bland-Altman plot between the ground-truth HR (ECG) and the calculated HR (PPG) is shown in Fig.11(b). The Limit of Agreement (LOA) is [-5.54, 6.19] beats/min with standard deviation σ : 2.99 in the two sessions, and 95% of all differences are inside this range. Fig.11(a) illustrates the scatter plot between the ground-truth HR and the related estimates on 12 subjects in LU-Db with the Pearson Correlation r : 0.9953.

Table 2 illustrates the ϵ_1 values of RR in the 1st and 2nd sessions for

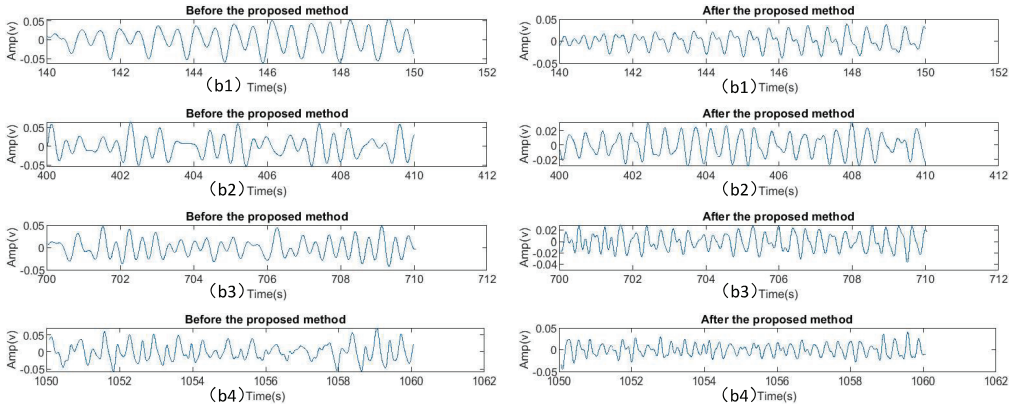

Fig. 10. Detailed PPG signals in the time domain correspond to different points in Fig.8(b).

	Subj	F01	F02	F03	M04	M05	M06	M07	M08	M09	M10	M11	M12
1st	ϵ_1	0.91	1.16	1.15	0.93	1.01	1.25	1.04	0.73	1.21	1.32	1.22	0.93
	ϵ_2	0.72	1.10	0.99	0.97	0.79	1.18	1.07	0.91	1.12	1.37	1.40	0.88
2nd	ϵ_1	1.52	1.47	1.16	1.35	1.31	1.37	1.37	1.49	1.27	2.19	1.67	1.78
	ϵ_2	1.08	1.03	0.90	1.02	1.10	1.05	1.18	1.48	1.02	2.11	1.58	1.60

Table 1: Average Absolute Error (ϵ_1) (in beats/min) and Average Absolute Error Percentage ($\epsilon_2(\%)$) on all 12 subjects (F-female, M-male) of LU-Db with different sessions.

12 subjects, and average ϵ_1 in different sessions are 2.56 ± 0.34 (mean $\pm$ std) and 2.99 ± 0.15 (mean $\pm$ std) breaths/min, respectively. Fig. 12(a) displays the scatter plot between the ground-truth and calculated RR on 12 subjects in LU-Db with the Pearson Correlation r : 0.9269. Additionally, the Bland-Altman plot is applied for all 12 subjects, is given in Fig. 12(b). The LOA between the ground-truth and the calculated RR data is [-6.41, 6.87] breath/min.

	Subj	F01	F02	F03	M04	M05	M06	M07	M08	M09	M10	M11	M12
1st	ϵ_1	3.07	2.16	2.25	2.81	2.41	3.16	2.24	2.17	2.65	2.79	2.47	2.64
2nd	ϵ_1	2.94	2.95	2.72	2.81	3.17	3.23	3.17	3.09	2.96	3.01	2.86	3.02

Table 2: Average Absolute Error (ϵ_1) (in breaths/min) on all 12 subjects (F-female, M-male) of LU-Db datasets with different sessions.

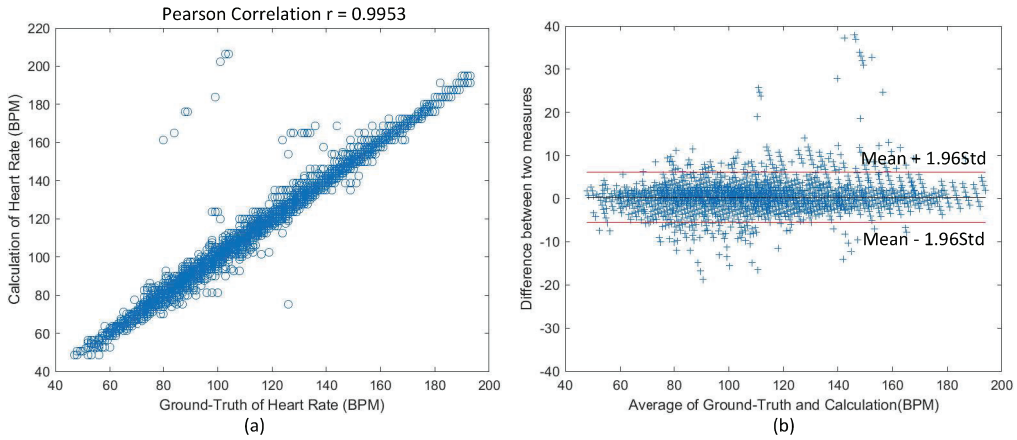

Fig. 11. HR calculation results on 12 subjects of LU-Db with 1st and 2nd sessions (BPM: beats/min). (a) Pearson correlation plot. (b) Bland-Altman plot.

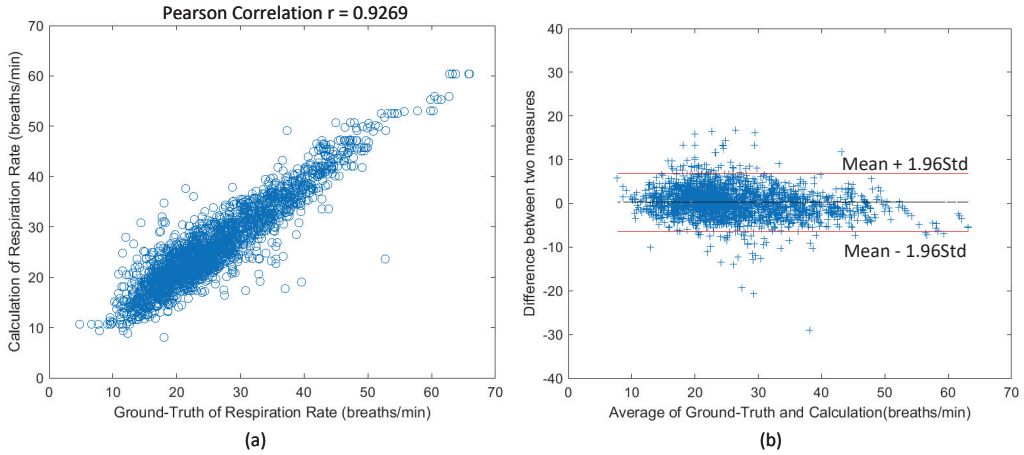

Fig. 12. RR calculation results on 12 subjects of LU-Db with 1st and 2nd sessions. (a) Pearson correlation plot. (b) Bland-Altman plot.

3.2. Results Comparison

To better represent the performance of the ANF, the IEEE-SPC dataset is adopted as a benchmark for comparison of the proposed algorithm with other recently reported algorithms as shown in Table 3. It is observed that the ANF performance exceeds that of the other algorithms in terms of overall mean error (ϵ_1). Table 4 shows that the ANF has fewer tunable parameters

compared to other algorithms listed. Fewer user-tunable parameters could simplify the complexity of the algorithm and improve the generalization performance on other datasets.

Subject	TROIKA [20]	Wang [24]	MUARD [16]	Zhao. [6]	Arunkumar et al. [28]	Zhang. [29]	ANF
1	2.29	1.09	1.17	1.23	1.13	2.06	1.08
2	2.19	0.87	0.93	1.51	0.87	3.59	0.94
3	2.00	1.20	0.70	1.19	0.73	0.92	0.74
4	2.15	0.81	0.82	0.92	0.95	1.54	0.75
5	2.01	0.67	0.88	0.61	0.85	0.97	0.69
6	2.76	1.15	0.97	0.78	0.94	1.64	0.89
7	1.67	0.73	0.67	0.48	0.66	2.25	0.73
8	1.93	0.49	0.74	0.56	0.70	0.63	0.60
9	1.86	0.34	0.49	0.49	0.59	0.62	0.61
10	4.70	2.06	2.69	3.81	3.94	4.62	1.94
11	1.72	0.87	0.81	0.78	1.01	1.30	0.92
12	2.84	0.78	0.77	1.04	0.95	1.80	0.99
Mean (Std)	2.32 (0.84)	0.92 (0.44)	0.97 (0.57)	1.06 (0.91)	1.11 (0.90)	1.83 (1.21)	0.91 (0.36)

Table 3: Average Absolute Error (ϵ_1) (in beats/min) on the IEEE-SPC of the ANF along with the same of other recently reported results.

Tunable threshold	TROIKA [20]	Wang [24]	MUARD [16]	Zhao. [6]	Arunkumar et al. [28]	Zhang. [29]	ANF
MA-Removal	>10	5	6	>10	>10	6	4
HR tracking and validation	>10	4	2	2	3	2	2

Table 4: The number of user-tunable parameters in MA-removal and HR tracking and validation steps.

3.3. Feasibility of Real-time Signal Processing

To perform the ANF algorithm in the near-real-time situation, the memory size of the embedded system is considered to be a crucial indicator to evaluate the algorithm portability. The computational complexity depends more on the FFT operation in ANF algorithm. Specifically, the ANF adopted four N_{FFT}-point FFTs with zero padding operations, i.e., ACC spectrum, PPG spectrum, HR calculation and RR calculation, and N_{FFT}-point was set 8192. According to the actual embedded memory and clock cycle, taking ARM Cortex-M4 as an example, it supports a maximum of 1024-point

FFT operations and the required block size is 139,898 bytes. ANF with 8192-point FFT cannot meet the computing and memory requirements of embedded systems. Thus, ANF with 1024-point FFT would be applied to achieve the near-real-time signal processing through the downsampling. In other words, the sampling rate of LU-Db dataset is 256 Hz, which means that the 2560 samples would be collected in each 10s sliding window. In order to meet the actual embedded memory requirements, the sampling rate needs to be reduced to 64 Hz to perform the 1024-point FFT operation. Therefore, four 1024-point FFTs required $4 * 139898 \approx 0.5M$ clock cycles, and the ARM Cortex-M4 can run at 100 MHz that means a hundred FFTs is not much of a problem. The comparison result of ANF with 1024-point FFT and 8192-point FFT is as follows.

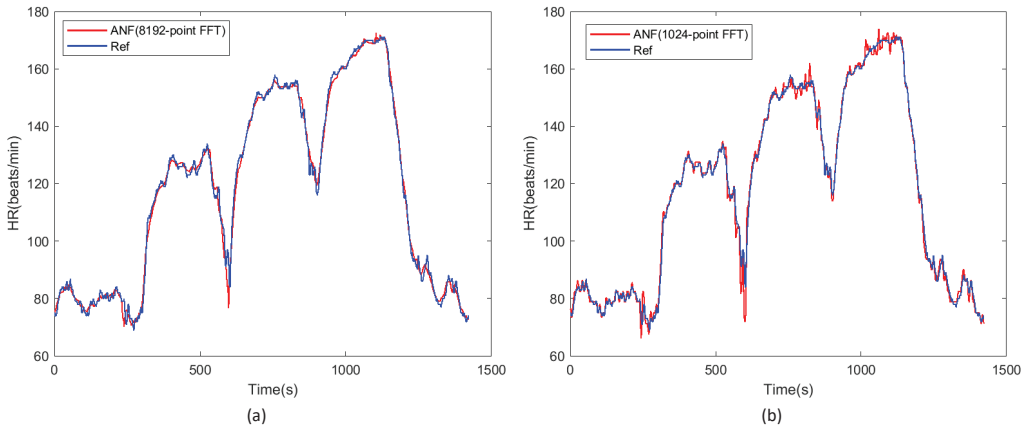

Fig. 13. The comparison result of ANF with 1024-point FFT and 8192-point FFT on M011 subject chosen LU-Db datasets. (a) ANF with 8192-point FFT. (b) ANF with 1024-point FFT.

4. Discussion

Although the acceleration-based adaptive filter could improve the accuracy of HR calculation, such adaptive filters are still dependent on the signal quality of the reference acceleration signal [28]. The previous study [19] had addressed this issue by proposing the bandstop filter based on the 3-axis acceleration reference, the work was mainly proposed to address the motion scenarios with lower intensity. The ANF described in the present study has

effectively removed MAs and recovered cleansed PPG signals using a reference signal from the 3-axis accelerometer at different motion intensities. In spite of the application of bandstop or notch filters, in noise-free PPG signal extraction, having been used before [1] [24], the calculation accuracy still needs to be improved. In this study, the proposed solution creates a algorithm to accurately extract HR and RR, and provides a flexible combination of the notch filter to retain physiological information in these PPG signal datasets, making it easier to extract accurate physiological parameters. At this point, ANF could represent an improved solution for embedded, real-time, wearable detection devices due to the low complexity.

Compared with other algorithms, the ANF has an improved HR/RR calculation performance. Specifically, the adaptability of the ANF gives it an advantage for removing MAs in different motion intensities, much superior to fixed bandstop filters [1]. Table 3 presents the better performance of ANF for the IEEE-SPC dataset. Although the average error result of the ANF is only marginally better (0.01 beats/min) than method in [24], the error between datasets (*std*) is lower than in [24]. Additionally, the ANF shows it is capable of extracting accurate HR at four stages of increasing intensity on a cycle ergo-meter and a treadmill compared to standard commercial devices.

Conversely, the accuracy of RR extraction has a larger ϵ_1 compared to the HR measurement, which is 2.56 ± 0.34 and 2.99 ± 0.15 breaths/min in cycling and treadmill exercises with different motion intensities. On the other hand, the RR is located in a much lower frequency range (0.1–1.0 Hz), and it is more susceptible to interference from MAs than HR measurement [30]. As shown in Fig.7, the measured RR was broadly consistent with the reference RR trend, and it also shows the stepwise increase with increasing exercise intensity. Again, to make the ANF algorithm more lightweight, a low-complexity and efficient method is adopted for RR extraction, but it could reduce the extraction accuracy.

Furthermore, the methods as reported in Table 4 follows a number of heuristic rules and thresholds. For instance, the MA removal as presented in [20], [24], [16], [6], [28] and [29] requires several and defined parameters. Increasing the tunable parameters of designated algorithms could lead to an improved performance but it could increase complexity of signal processing and lead a risk of poor generalization on physiological monitoring datasets with MAs. Although the present ANF runs on a PC, its performance has demonstrated that the ANF could be easily deployed onto a wearable embedded platform in consolidating with the mOEPS.

5. Conclusion

This study has demonstrated that the ANF that has been developed can accurately remove of MAs allowing for the extraction of two physiological parameters, i.e., HR and RR, for health monitoring during physical activity/exercise, by the utilization the mOEPS.

The ANF processing procedures, as described in the section on Methodology and Materials, demonstrates the removal of MA using a low complexity and intuitive method, thus making real-time signal processing achievable. With the ANF, the AMAF plays a critical role in removing out-of-band noise, and the adaptive notch filter works on the removal of in-band noise by the means of 3-axis acceleration reference. HR and RR, as critical physiological parameters, are obtained with a sliding time window, thus recovering the distinctive PPG signals.

The proposed ANF has been applied to the LB-Db and IEEE-SPC datasets to deliver improved accuracy for HR and RR readings compared to other methods in the literature. These results have illustrated that the ANF could effectively recover the desired PPG signals with apparent features, in real-time, even when the subject was exercising at different intensities.

Acknowledgments

The authors would like to acknowledge the support of Loughborough University in the conduction of this study, and the shared the datasets from the IEEE-SPC.

Conflict of interest

The authors declare that there is no any conflict of interest for this study.

Author Contributions

XZ carried out the study, the data processing, and wrote the manuscript. VMD provided background knowledge and advised on original work, co-supervised the study. MD jointly supervised the study and reviewed the manuscript. LB provided exercise protocol and advised on original work, co-supervised the study. SH structured the manuscript, analyzed the outcomes, and supervised the study.

References

[1] S. Nabavi, S. Bhadra, A robust fusion method for motion artifacts reduction in photoplethysmography signal, IEEE Trans. Instrum. Meas. 69 (12) (2020) 9599–9608, doi:http://doi.org/10.1109/TIM.2020.3006636.

[2] M. Schmidt, A. Schumann, J. Miller, K.-J. Bar, G. Rose, ECG derived respiration: Comparison of time-domain approaches and application to altered breathing patterns of patients with schizophrenia, Physiol. Meas. 38 (2017) 601–, doi:http://doi.org/10.1088/1361-6579/aa5feb.

[3] W. Lin, D. Wu, C. Li, H. Zhang, Y. Zhang, Comparison of heart rate variability from PPG with that from ECG, Int Conf on Health Inform. 42 (2017) 213–215, doi:http://doi.org/10.1007/978-3-319-03005-$0_5$4.

[4] D. Biswas, N. Simões-Capela, C. Van Hoof, N. Van Helleputte, Heart rate estimation from wrist-worn photoplethysmography: A review, IEEE Sensors J. 19 (2019) 6560–6570, doi:http://doi.org/10.1109/JSEN.2019.2914166.

[5] H. Chung, H. Lee, J. Lee, Finite state machine framework for instantaneous heart rate validation using wearable photoplethysmography during intensive exercise, IEEE J. Biomed. Health Inform. 23 (4) 1595–1606, doi:http://doi.org/10.1109/JBHI.2018.2871177.

[6] D. Zhao, Y. Sun, S. Wan, F. Wang, Sfst: A robust framework for heart rate monitoring from photoplethysmography signals during physical activities, Biomed. Signal Process. Control 33 (2017) 316–324, doi:http://doi.org/10.1016/j.bspc.2016.12.005.

[7] N. K. L. Murthy, P. C. Madhusudana, P. Suresha, V. Periyasamy, P. K. Ghosh, Multiple spectral peak tracking for heart rate monitoring from photoplethysmography signal during intensive physical exercise, IEEE Signal Process. Lett. 22 (12) (2015) 2391–2395, doi:http://doi.org/10.1109/LSP.2015.2486681.

[8] B. S. Kim, S. K. Yoo, Motion artifact reduction in photoplethysmography using independent component analysis, IEEE Trans. Biomed. Eng. 53 (3) (2006) 566–568, doi:http://doi.org/10.1109/TBME.2005.869784.

[9] R. Krishnan, B. Natarajan, S. Warren, Two-stage approach for detection and reduction of motion artifacts in photoplethysmographic data, IEEE Trans. Biomed. Eng. 57 (8) (2010) 1867–1876, doi:http://doi.org/10.1109/TBME.2009.2039568.

[10] E. Khan, F. Al Hossain, S. Z. Uddin, S. K. Alam, M. K. Hasan, A robust heart rate monitoring scheme using photoplethysmographic signals corrupted by intense motion artifacts, IEEE Trans. Biomed. Eng. 63 (3) (2015) 550–562, doi:http://doi.org/10.1109/TBME.2015.2466075.

[11] M. A. Motin, C. K. Karmakar, M. Palaniswami, Selection of empirical mode decomposition techniques for extracting breathing rate from ppg, IEEE Signal Process. Lett. 26 (4) (2019) 592–596, doi:http://doi.org/10.1109/LSP.2019.2900923.

[12] M. Raghuram, K. V. Madhav, E. H. Krishna, K. A. Reddy, Evaluation of wavelets for reduction of motion artifacts in photoplethysmographic signals, in: 10th Int. Conf. Inf. Sci., Signal Process. Their Appl. (ISSPA 2010), 2010, pp. 460–463, doi:http://doi.org/10.1109/ISSPA.2010.5605443.

[13] A. Galli, C. Narduzzi, G. Giorgi, Measuring heart rate during physical exercise by subspace decomposition and kalman smoothing, IEEE Trans. Instrum. Meas. 67 (5) (2017) 1102–1110, doi:http://doi.org/10.1109/TIM.2017.2770818.

[14] A. Koneshloo, D. Du, A novel motion artifact removal method via joint basis pursuit linear program to accurately monitor heart rate, IEEE Sensors J. 19 (21) (2019) 9945–9952, doi:http://doi.org/10.1109/JSEN.2019.2927994.

[15] H. Fukushima, H. Kawanaka, M. S. Bhuiyan, K. Oguri, Estimating heart rate using wrist-type photoplethysmography and acceleration sensor while running, in: Conf IEEE Eng Med Bio Soc (EMBC), 2012, pp. 2901–2904, doi:http://doi.org/10.1109/EMBC.2012.6346570.

[16] S. S. Chowdhury, R. Hyder, M. S. B. Hafiz, M. A. Haque, Real-time robust heart rate estimation from wrist-type ppg signals using multiple reference adaptive noise cancellation, IEEE J. Biomed. Health Inform. 22 (2) (2016) 450–459, doi:http://doi.org/10.1109/JBHI.2016.2632201.

[17] M. R. Ram, K. V. Madhav, E. H. Krishna, N. R. Komalla, K. A. Reddy, A novel approach for motion artifact reduction in ppg signals based on as-lms adaptive filter, IEEE Trans. Instrum. Meas. 61 (5) (2011) 1445–1457, doi:http://doi.org/10.1109/TIM.2011.2175832.

[18] R. Yousefi, M. Nourani, S. Ostadabbas, I. Panahi, A motion-tolerant adaptive algorithm for wearable photoplethysmographic biosensors, IEEE J. Biome. Health Inform. 18 (2) (2013) 670–681, doi:http://doi.org/10.1109/JBHI.2013.2264358.

[19] S. Nabavi, S. Debbarma, S. Bhadra, Measurement of cardiac parameters by motion artifacts free photoplethysmography signals, in: Conf IEEE Int. Instrum. Meas. Technol. (I2MTC), 2020, pp. 1–6, doi:http://doi.org/10.1109/I2MTC43012.2020.9128713.

[20] Z. Zhang, Z. Pi, B. Liu, Troika: A general framework for heart rate monitoring using wrist-type photoplethysmographic signals during intensive physical exercise, IEEE Trans. Biomed. Eng. 62 (2) (2014) 522–531, doi:http://doi.org/10.1109/TBME.2014.2359372.

[21] Z. Zhang, Photoplethysmography-based heart rate monitoring in physical activities via joint sparse spectrum reconstruction, IEEE Trans. Biomed. Eng. 62 (8) (2015) 1902–1910, doi:http://doi.org/10.1109/TBME.2015.2406332.

[22] S. Salehizadeh, D. Dao, J. Bolkhovsky, C. Cho, Y. Mendelson, K. H. Chon, A novel time-varying spectral filtering algorithm for reconstruction of motion artifact corrupted heart rate signals during intense physical activities using a wearable photoplethysmogram sensor, Sensors 16 (1) (2016) 10, doi:http://doi.org/10.3390/s16010010.

[23] M. T. Islam, S. T. Ahmed, C. Shahnaz, S. A. Fattah, Specmar: Fast heart rate estimation from ppg signal using a modified spectral subtraction scheme with composite motion artifacts reference generation, Med. Biol. Eng. Comput. 57 (3) (2019) 689–702, doi:http://doi.org/10.1007/s11517-018-1909-x.

[24] M. Wang, Z. Li, Q. Zhang, G. Wang, Removal of motion artifacts in photoplethysmograph sensors during intensive exercise for accurate heart

rate calculation based on frequency estimation and notch filtering, Sensors 19 (15) (2019) 3312, doi:http://doi.org/10.3390/s19153312.

[25] C.-C. Tseng, S.-C. Pei, Stable iir notch filter design with optimal pole placement, IEEE Trans. Signal Process. 49 (11) (2001) 2673–2681, doi:http://doi.org/10.1109/78.960414.

[26] G.-Z. Liu, Y.-W. Guo, Q.-S. Zhu, B.-Y. Huang, L. Wang, Estimation of respiration rate from three-dimensional acceleration data based on body sensor network, Telemed. E-health 17 (9) (2011) 705–711, doi:http://doi.org/10.1089/tmj.2011.0022.

[27] A. Alzahrani, S. Hu, V. Azorin-Peris, L. Barrett, D. Esliger, M. Hayes, S. Akbare, J. Achart, S. Kuoch, A multi-channel opto-electronic sensor to accurately monitor heart rate against motion artefact during exercise, Sensors 15 (10) (2015) 25681–25702, doi:http://doi.org/10.3390/s151025681.

[28] K. Arunkumar, M. Bhaskar, Heart rate estimation from wrist-type photoplethysmography signals during physical exercise, Biom. Signal Process. Control 57 (2020) 101790, doi:http://doi.org/10.1016/j.bspc.2019.101790.

[29] Y. Zhang, B. Liu, Z. Zhang, Combining ensemble empirical mode decomposition with spectrum subtraction technique for heart rate monitoring using wrist-type photoplethysmography, Biomed. Signal Process. Control 21 (2015) 119–125, doi:http://doi.org/10.1016/j.bspc.2015.05.006.

[30] P. Kuwalek, B. Burlaga, W. Jesko, P. Konieczka, Research on methods for detecting respiratory rate from photoplethysmographic signal, Biomed. Signal Process. Control 66 (2021) 102483, doi:http://doi.org/10.1016/j.bspc.2021.102483.